Plasticity and Damage Modeling of the AA7075 Aluminium Alloy for Hot Stamping

G. D'Amours
National Research Council Canada, Aluminium Technology Centre, Saguenay, Canada
A. Ilinich
Ford Research and Innovation Center, Dearborn, Michigan, USA

Abstract

*LS-DYNA® has several plane stress material models available for isothermal aluminum sheet stamping, most notably *MAT_3-PARAMETER_BARLAT, *MAT_BARLAT_YLD2000, and *MAT_KINEMATIC_HARDENING_BARLAT89. Recent models such as *MAT_BARLAT_YLD2000 based on Barlat's YLD2000 yield surface accurately capture plastic flow and yield anisotropy of most aluminum sheet alloys. Some of these models are also applicable for non-isothermal forming. However, there are no general stress state models available for solid elements that can describe aluminum anisotropy and support temperature and rate depended parameters and hardening. Another problem is failure prediction as there are no temperature and rate sensitive failure criteria available for hot forming. This paper presents the development, implementation and validation of a user defined material model (UMAT) for the AA7075 aluminium hot stamping process which supports both shell and solid elements. It includes Hill plasticity with a non-associated flow rule and a damage model similar to GISSMO but extended to cover non-isothermal conditions. All simulations were performed using the implicit thermal and mechanical solvers in LS-DYNA which has several features for hot stamping modeling.*

Introduction

Some automotive manufacturers are now intensively using aluminium alloys to reduce vehicles weight. For BIW applications, one potential process that is receiving more attention recently is the aluminium hot stamping. This process can be used for 6000 and 7000 series aluminium alloys but is especially beneficial for high strength 7000 series which are difficult to form otherwise. Some researchers such as Harrison *et al.* [1], Xiao *et al.* [2] and Kumar *et al.* [3] have started to work on this process and have formed high strength prototype parts. In this process, the sheet is solutionized before the stamping operation. The process is carried out in non-isothermal conditions where die is cooled to almost room temperature. As aluminium alloys have a high thermal conductivity, the stamping step must be completed within few seconds to avoid forming "cold" material.

Modeling hot forming is more complicated than modeling conventional stamping. The non-isothermal hot stamping process requires inclusion of the temperature and strain rate dependent plasticity and damage properties in the model. Ilinich *et al.* [4] demonstrated that coupled thermo-mechanical non-isothermal hot forming models are more accurate than conventional purely mechanical isothermal models. One area of significant importance with very limited prior research is failure criteria for aluminum hot forming. FLD based approaches are inapplicable due to their inability to account for temperature and strain rate changes during the hot stamping process. Another popular choice in LS-DYNA is GISSMO which is a phenomenological damage accumulation model capable to predict both plastic instability and fracture. However, its current implementation is limited to isothermal conditions. Therefore, new models are necessary for the finite element analysis of the aluminum hot stamping process that take into account evolution of anisotropy, strain hardening and damage of aluminum sheet due to large temperature, strain rate, and loading path variations observed during this process.

LS-DYNA has excellent room temperature plane stress plasticity and damage models for forming applications but has only few high temperature plasticity models and almost no high temperature damage models. It has also limited 3D anisotropic plasticity models for aluminium alloys. For these reasons, a novel user material model (UMAT) have been developed, implemented and validated with hot stamping tests. UMAT model included both plasticity and damage models that are temperature, strain rate and loading path dependent, and support both plane stress and 3D element formulations. This paper presents the main characteristics of this UMAT for finite element analysis of the hot stamping of an AA7075 aluminium alloy.

Material of study and its characterization

The material of study was AA7075 aluminium sheet with thickness of 2 mm and chemical composition shown in Table 1 [1]. The sheet was received in T6 temper.

Table 1. Chemical composition of AA7075 aluminium sheet

Elements	Al	Cr	Cu	Fe	Mg	Mn	Si	Ti	Zn	Other, Each	Other, total
Wt. (%)	87.1-91.4	0.18-0.28	1.2-2.0	Max. 0.5	2.1-2.9	Max. 0.3	Max. 0.4	Max. 0.2	5.1-6.1	Max. 0.05	Max. 0.15

An extensive mechanical characterization was performed using isothermal uniaxial tensile test with ASTM E21 specimen geometry in a temperature range from 200 to 480 °C and strain rates from 0.01 to 10 s^{-1}. The heat treatment paths, shown in Figure 1, were designed to replicate the thermo-mechanical history of a typical hot stamping process. Material was first solution heat treated for 12 minutes, followed by a salt bath quench to the specific test temperature. After quenching the samples were tested to failure in an environmental chamber. The R-values were determined as described in D'Amours *et al.* [5].

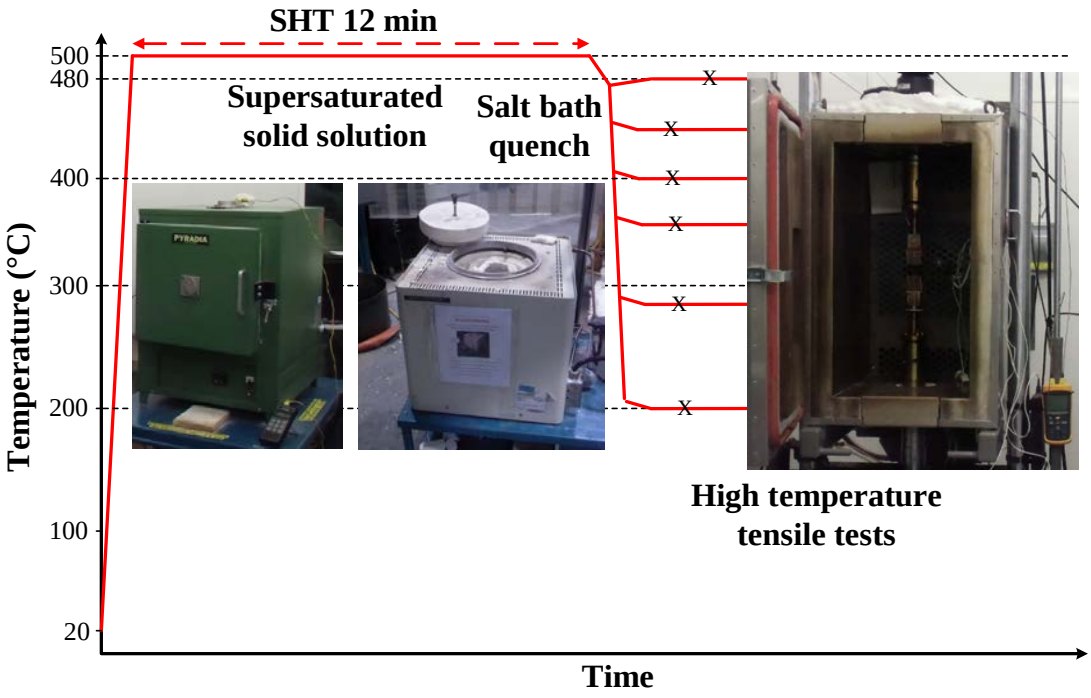

Figure 1. Heat treat path and equipment used for hot tensile tests

Figure 2 compares the experimental tensile curves for one strain rate (0.1 s^{-1}) in the left graph and for one temperature (400 °C) in the right graph, highlighting a significant temperature and rate dependency of 7075 alloy. As can be seen in the left graph, the 7075 sheet exhibited almost perfectly plastic flow with no strain hardening at temperatures above 280 °C and significant strain hardening at lower temperatures. The flow stress was observed to monotonically decrease with temperature and increase with strain rate. While total elongations were decreasing with strain rate, the effect of temperature was non-linear.

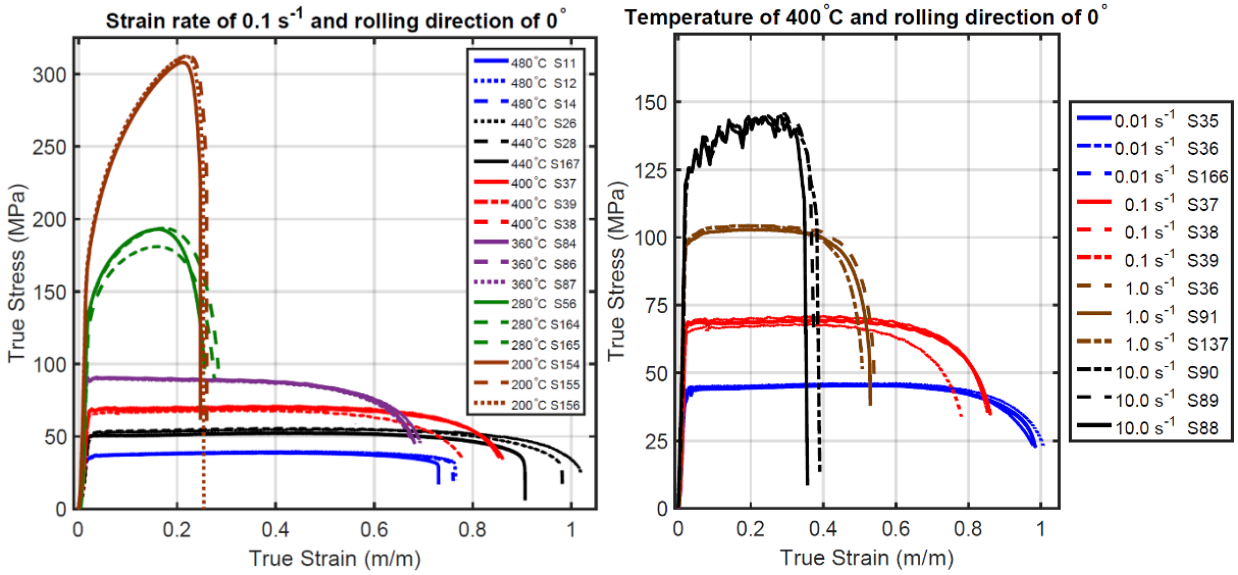

Figure 2. Stress-strain curves of the AA7075 showing temperature and strain rate dependences

Figure 3 demonstrates the stress and strain anisotropy of the 7075 sheet at 400 °C. The minimum flow stress was observed in the rolling direction (0°) and the maximum in the transverse direction (90°). The smallest R-value was also in the rolling direction. The stress anisotropy was small relatively to the strain anisotropy. The anisotropy behavior at other temperatures was similar.

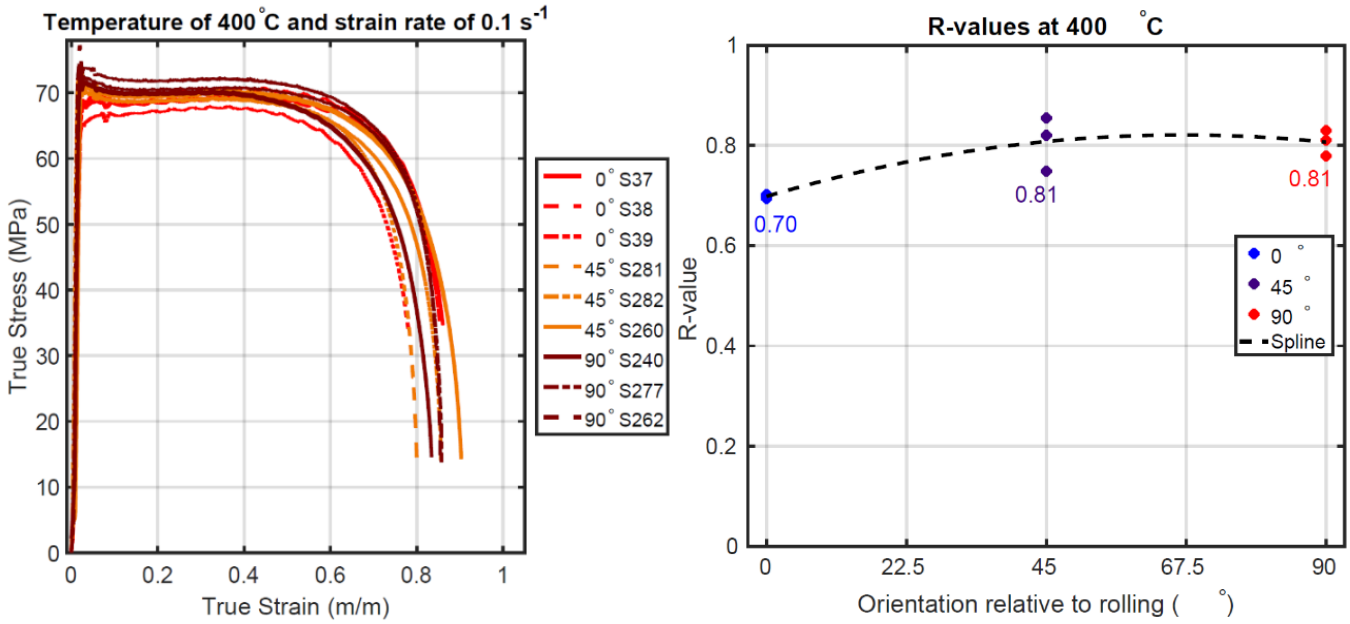

Figure 3. Stress and strain anisotropy of the AA7075 at 400°C and the strain rate of $0.1s^{-1}$

Formability characterization was performed using isothermal Nakazima test with the same thermal cycle as described above to determine the plastic instability strains and local fracture strains. The testing was performed over the same temperature and strain rate ranges using a graphite lubricant. Three loading paths were included in this study: uniaxial, plane strain and equibiaxial. Specimen geometries were optimized by finite element analysis (FEA). FEA was also used to determine punch displacement profiles for maintaining constant strain rates in the target areas of the blank. The Nakazima test setup is shown in Figure 4. Details on strain measurements are provided by D'Amours *et al.* [5].

Figure 4. High temperature Nakazima setup

Plasticity algorithm

One of the goals of the presented work was to create a general plasticity model applicable to both plane stress and 3D elements and able to accurately describe the observed anisotropic behavior as a function of temperature and strain rate. All these requirements can be satisfied by using a non-associated plastic flow rule (non-AFR) which has been used by D'Amours [6] to model plasticity of cohesive, porous and granular materials of aluminium reduction cells. In this model the plastic potential *Q* and the yield surface *F* are defined by two separate functions. Stoughton *et al.* [7] discussed potential advantage of non-AFR models for metals as well as stability conditions for unique and positively-definite plastic work. The non-AFR models with simple *Q* and *F* functions are in many cases less computationally expensive than more complex AFR models yet capture complex anisotropic behavior equally well or better. These models can be calibrated with just tensile tests and are suitable for 3D solid elements. Non-AFR models have been recently added in LS-DYNA [8].

Hill 1948 yield function [9] was selected in the present study for both the plastic potential function *Q* and the yield surface function *F*. The yield surface *F* for 3D solid elements was of the following form:

$$F = F_y(\sigma_{22} - \sigma_{33})^2 + G_y(\sigma_{33} - \sigma_{11})^2 + H_y(\sigma_{11} - \sigma_{22})^2 + 2L_y{\sigma_{23}}^2 + 2M_y{\sigma_{31}}^2 + 2N_y{\sigma_{12}}^2 - {S_y}^2 \quad (1)$$

where σ_{ij} are components of the stress tensor. F_y, G_y, H_y, N_y, L_y and M_y are the six coefficients of the Hill surface. To include planar stress anisotropy, anisotropy stress parameters $\sigma_0(T, \dot{\varepsilon})$, $\sigma_{45}(T, \dot{\varepsilon})$ and $\sigma_{90}(T, \dot{\varepsilon})$ were used as suggested by Wang *et al.* [10] to determine F_y, G_y, H_y, L_y, M_y and N_y parameters of the Hill 48 yield surface according to:

$$F_y = \frac{1}{2}\left(\frac{1}{{\sigma_{90}}^2} - \frac{1}{{\sigma_0}^2} + \frac{1}{{\sigma_z}^2}\right){S_{y0}}^2 \quad (2)$$

$$G_y = \frac{1}{2}\left(\frac{1}{{\sigma_0}^2} - \frac{1}{{\sigma_{90}}^2} + \frac{1}{{\sigma_z}^2}\right){S_{y0}}^2 \quad (3)$$

$$H_y = \frac{1}{2}\left(\frac{1}{{\sigma_0}^2} + \frac{1}{{\sigma_{90}}^2} - \frac{1}{{\sigma_z}^2}\right){S_{y0}}^2 \quad (4)$$

$$N_y = \left(\frac{2}{{\sigma_{45}}^2} - \frac{1}{2{\sigma_z}^2}\right){S_{y0}}^2 \quad (5)$$

$$M_y = L_y = N_y \quad (6\text{-}7)$$

In the UMAT, three different 2D tables were defined for the values of $\sigma_0(T, \dot{\varepsilon})$, $\sigma_{45}(T, \dot{\varepsilon})$ and $\sigma_{90}(T, \dot{\varepsilon})$. For six experimental temperatures and four strain rates, a total of 72 coefficients were necessary. All these parameters were defined from the experimental stress-strain curves. Parameter σ_z is the through thickness stress anisotropy and was assumed equal to σ_{90} due to the low level of stress anisotropy expected after solution heat treatment of the AA7075 aluminium alloy. S_{y0} is the yield stress in the rolling (0°) direction defined as a function of the equivalent plastic strain, the strain rate and the temperature in a form of a 3D table in UMAT. Linear interpolation was used for strain and temperature dependence and logarithmic interpolation was used for strain rate dependence. Examples of calibrated plane stress and 3D yield surfaces for the AA7075 are shown in Figure 5.

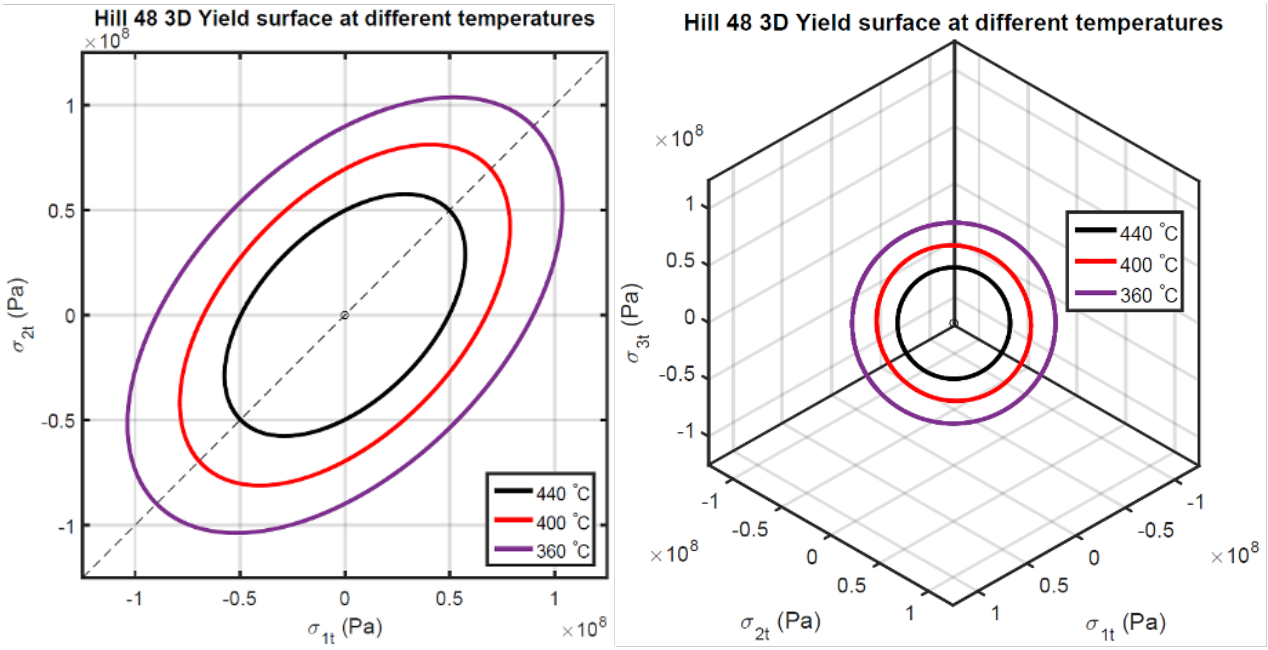

Figure 5. Yield surfaces of the AA7075 for different temperatures and the strain rate of 0.1s^{-1}

The plastic potential Q was defined by the same Hill 48 equation but with a different set of parameters to predict the direction of plastic deformations:

$$Q = F_p(\sigma_{22} - \sigma_{33})^2 + G_p(\sigma_{33} - \sigma_{11})^2 + H_p(\sigma_{11} - \sigma_{22})^2 + 2L_p{\sigma_{23}}^2 + 2M_p{\sigma_{31}}^2 + 2N_p{\sigma_{12}}^2 - {S_y}^2 \quad (8)$$

In order to include planar strain anisotropy, R-value parameters $R_0(T)$, $R_{45}(T)$ and $R_{90}(T)$ were used according to Kami *et al.* [11] to determine F_p, G_p, H_p, L_p, M_p and N_p parameters of the Hill 48 plastic potential:

$$H_p = \frac{R_0}{(R_0+1)} \quad (9)$$

$$F_P = \frac{H_p}{R_{90}} \quad (10)$$

$$G_p = \frac{H_p}{R_0} \quad (11)$$

$$N_y = \frac{(R_0+R_{90})(2R_{45}+1)}{2R_{90}(R_0+1)} \quad (12)$$

$$M_p = N_p = \frac{3}{2} \quad (13\text{-}14)$$

A 2D table was used to define R-value function of temperature and the loading direction in the UMAT. Examples of plane stress and 3D plastic potentials for the AA7075 at two temperatures are shown in Figure 6. A significant departure from the isotropic von Mises shape can be seen in both cases. Also, a slight rotation of the plastic potential between the temperatures can be noted in the left graph.

The integration of the plasticity algorithm was done with a full backward Euler schema. More details can be found in Crisfield [12] and D'Amours [6]. For the 3D algorithm, six components of strains and stresses were used. For the place stress model, three components of strains and stresses were used but the local thickness strain ε_{33} was computed as required by the LS-DYNA solver using the volume constancy relationship between the strain increments: $d\varepsilon_{33}^p = -(d\varepsilon_{11}^p + d\varepsilon_{22}^p)$.

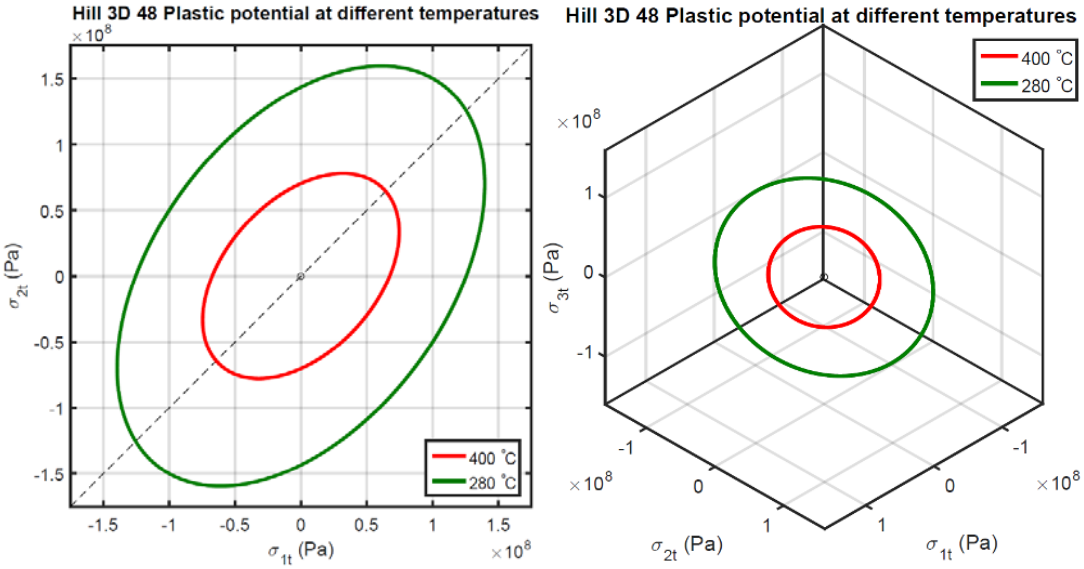

Figure 6. Plastic potentials of the AA7075 for different temperatures and the strain rate of $0.1s^{-1}$

Damage and fracture algorithms

A phenomenological damage accumulation framework was selected in this study to predict both plastic instability and fracture. A model similar to GISSMO [13] but with temperature and rate sensitivity was developed and included in the user material subroutine. In the UMAT, plasticity and damage algorithms were decoupled and damage parameters were computed upon convergence of the plasticity algorithm. As in GISSMO, two scalar variables, $D \in [0,1]$ and $IM \in [0,1]$, were introduced for fracture and instability risk accumulation respectively. An increment of fracture risk variable D was computed as following:

$$\Delta D = dx \left(\frac{\varepsilon_p}{\varepsilon_f(T,\dot{\varepsilon},\xi,\eta)}\right)^{(dx-1)} \left(\frac{\Delta\varepsilon_p}{\varepsilon_f(T,\dot{\varepsilon},\xi,\eta)}\right) \tag{15}$$

where ε_p and $\Delta\varepsilon_p$ are the equivalent plastic strain and its increment, dx is the damage exponent for non-linear damage accumulation, ε_f is the fracture strain that depends of the temperature T, the strain rate $\dot{\varepsilon}$, the stress triaxiality η, defined in equation 16, and the Lode angle parameter ξ, defined in equation 17.

$$\eta = \frac{\sigma_m}{\sigma_{vM}} \tag{16}$$

$$\xi = 1 - \frac{2}{\pi}\cos^{-1}\left(\frac{\sqrt{27}}{2}\frac{J_3}{J_2^{\frac{3}{2}}}\right) \tag{17}$$

where σ_m, σ_{vM}, J_2 and J_3 are classical stress invariants. The Lode angle parameter was an independent variable only in the model for 3D elements as there is a unique relationship between ξ and η in plane stress case shown by Bai *et al.* [14]. Therefore for shell model, ξ was computed using:

$$\xi = 1 - \frac{2}{\pi}\cos^{-1}\left(-\frac{27}{2}\eta\left(\eta^2 - \frac{1}{3}\right)\right) \tag{18}$$

The second scalar parameter, the instability measure IM, was incremented using:

$$\Delta IM = dx \left(\frac{\varepsilon_p}{\varepsilon_i(T,\dot{\varepsilon})}\right)^{(dx-1)} \left(\frac{\Delta\varepsilon_p}{\varepsilon_i(T,\dot{\varepsilon})}\right) \tag{19}$$

where ε_i is the instability strain that depends of the temperature T, the strain rate $\dot{\varepsilon}$. Stress coupling was implemented for the post-instability response ($IM \geq 1$) to insure a gradual decrease of load bearing capacity to *0* when the value of damage parameter D reaches unity. This was achieved by the following update to the uncoupled stress vector $\vec{\sigma}$:

$$\vec{\sigma}_{Dmg} = \left(1 - \left(\frac{D_{new} - D_{crit}}{1 - D_{crit}}\right)^{fx}\right)\vec{\sigma} \tag{20}$$

where fx is the fade exponent for stress coupling and *Dcrit* is a constant which value is equal to *D* when the instability *IM* reaches the value of *1.0*.

The instability strain $\varepsilon_i(T, \dot{\varepsilon})$ was determined directly from the hot tensile test results and used in UMAT in a form of a 2D table. While ε_i was assumed independent of stress triaxiality η and the Lode angle parameter ξ, the model can be easily expanded to include this dependence. Fracture surfaces $\varepsilon_f(\xi, \eta)$ were assumed to have shape proposed by Bai *et al.* [14]:

$$f_1 = \cos\left(\frac{\xi\pi}{6}\right) \tag{21}$$

$$f_2 = \sin\left(\frac{\xi\pi}{6}\right) \tag{22}$$

$$c_\xi^{ax} = \begin{cases} 1 \ for \ \xi \geq 0 \\ c_\xi^c \ for \ \xi < 0 \end{cases} \tag{23}$$

$$f_3 = c_\xi^s + \frac{\sqrt{3}}{2-\sqrt{3}}\left(c_\xi^{ax} - c_\xi^s\right)\left(\frac{1}{f_1} - 1\right) \tag{24}$$

$$f_4 = \sqrt{\frac{1+{c_1}^2}{3}} f_1 + c_1\left(\eta + \frac{1}{3} f_2\right) \tag{25}$$

$$\varepsilon_f = (c_0 f_3 f_4)^{-\frac{1}{n}} \tag{26}$$

where c_ξ^s, c_0, c_1, c_ξ^c, and n are free parameters determined by minimizing the difference between the hot tensile and Nakazima experimental and simulation results for different paths. The identification of these parameters was done for each combination of temperature and strain rate. Finally, all parameters were expressed as functions of the temperature and the strain rate in the form of 2D tables in the UMAT.

Damage model calibration was performed for six temperatures (480, 440, 400, 360, 280 and 200 °C) and two strain rates (0.1 and 1.0 s^{-1}) using experimental results from three loading paths (uniaxial, plane strain and biaxial). An example comparison of Nakazima plane strain tests and simulation results at 480°C and a strain rate of 0.1 s^{-1} is given in Figures 7 and 8. The resultant fracture strain surfaces at different temperatures and at the lower strain rate are shown in Figure 9.

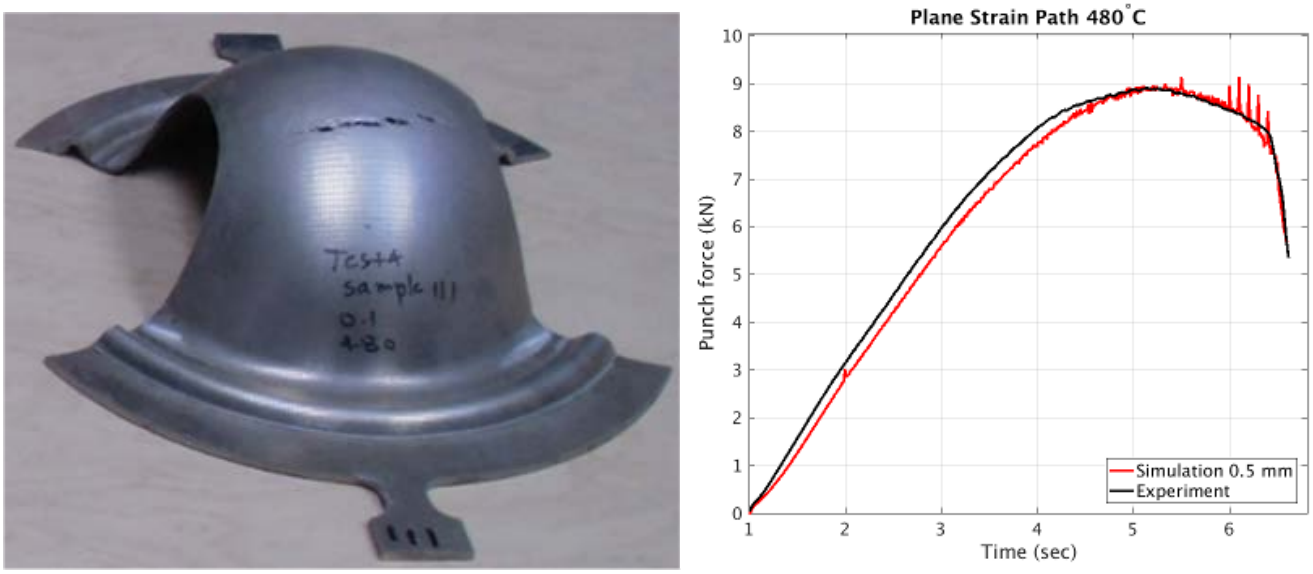

Figure 7. Example of a high temperature Nakazima test sample (left) and force measurement (right)

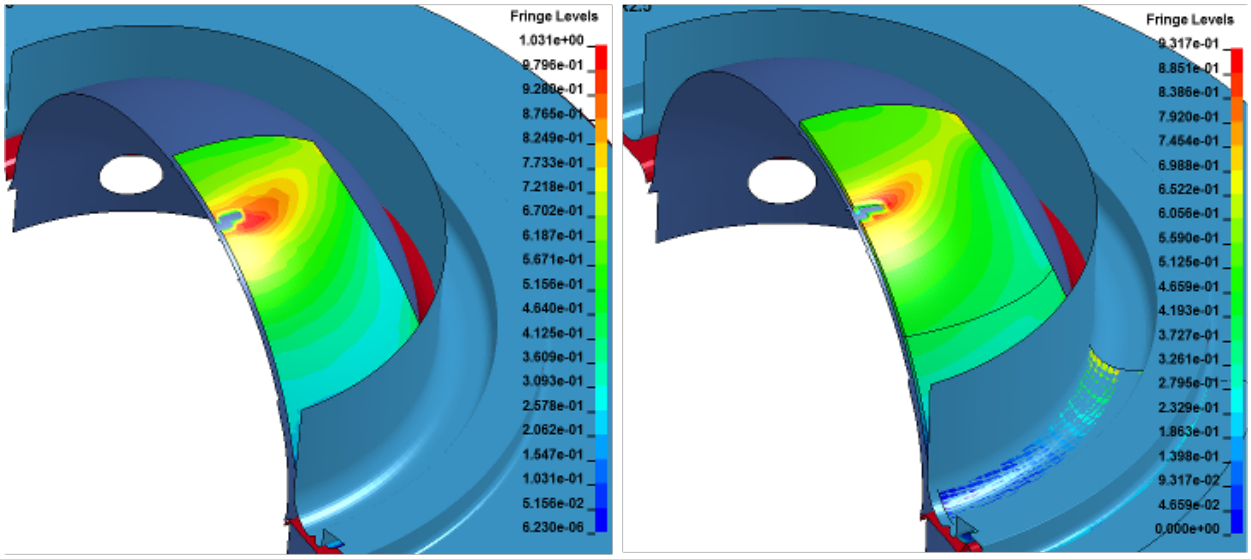

Figure 8. Example of a high temperature Nakazima simulation results with shell elements (left) and solid elements (right)

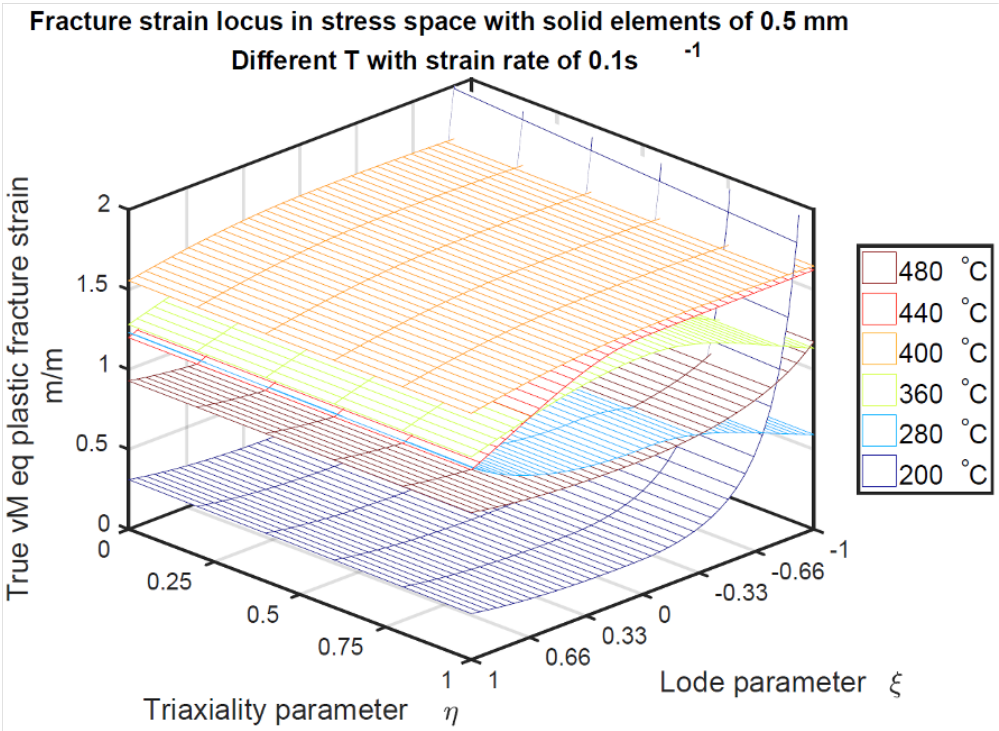

Figure 9. Calibrated fracture strain surfaces

Validation

Non-isothermal hot stamping trials with the AA7075 aluminium sheet have been executed with different experimental dies ranging from a water-cooled Nakazima die installed in a hydraulic MTS press as shown in Figure 10, up to a full size prototype die installed in a *1000 tons* hydraulic press. An infrared camera was used to measure blank temperature during stamping and quenching. Both the binder and the punch were water-cooled to increase repeatability and reduce cool-down time between the experiments. Black paint and graphite were added on both blank surfaces before the solution heat treatment. Validation tests were performed with various punch displacements, punch speeds and initial blank temperatures to obtain a variety of post-form conditions including successful, necked, and fractured parts.

Figure 10. Example of a hot stamping apparatus used for validation

Both the plane-stress and solid element models were applied to simulate the majority of the performed validations tests. Good agreement was observed between the simulation and experimental results. Figure 11 shows an example of a biaxial Nakazima sample hot stamped with settings to induce fracture. The equivalent plastic strain ε_p distribution predicted by the shell and solid models are shown in the bottom of Figure 11. Maximum equivalent strain values over *0.92 m/m* were reached at fracture. Predicted fracture location matched the experiment.

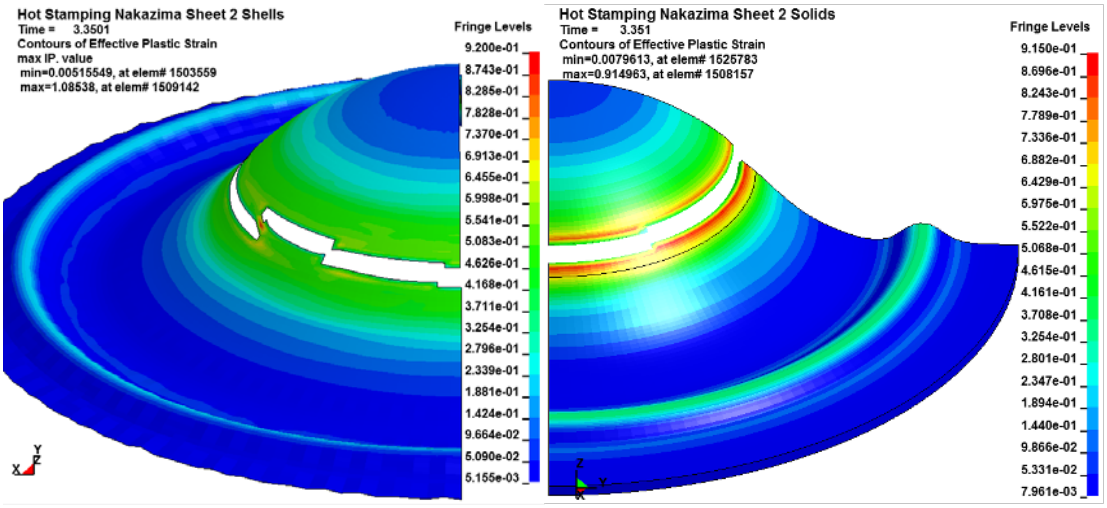

Figure 11. Biaxial sample hot stamped up to fracture. Predicted strains and fracture with shell (left) and solid elements (right)

Figure 12 shows an example of a plane strain Nakazima sample hot stamped with settings to induce necking. Also included in the figure is a distribution of the damage parameter *D* predicted by the plane stress model.

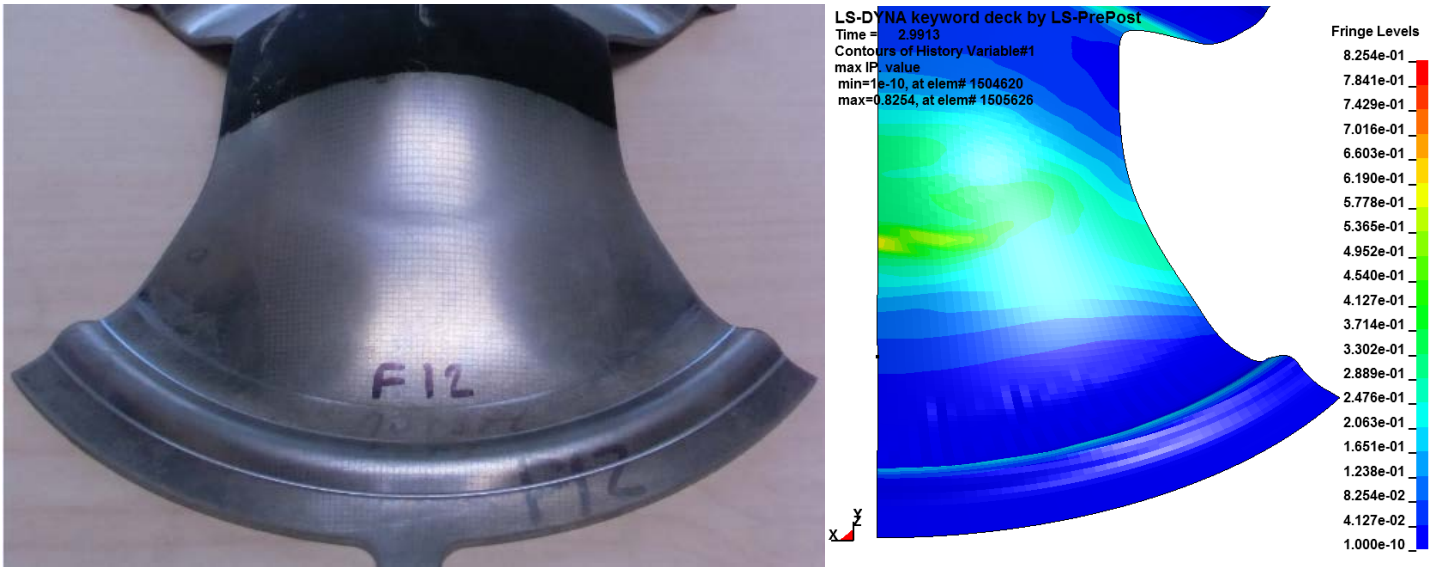

Figure 12. Plane strain sample hot stamped up to the appearance of a visible neck. Predicted damage distribution with shell elements

Conclusion

This paper presented an overview of a user material model developed for AA7075 aluminium hot stamping simulation. This custom material model was implemented in LS-DYNA for both plane-stress and solid elements. The non-associated flow rule was selected for plasticity and was shown to accurately describe the anisotropic plastic behavior of this alloy in a wide range of temperatures and strain rates. The model demonstrated excellent stability in implicit simulations with a substantial reduction of the computation time relative to explicit models. For damage and fracture treatment, a phenomenological GISSMO type model was implemented in this study. This conventional GISSMO model was extended by incorporating temperature and strain rate dependency. This approach demonstrated great potential in predicting both the plastic instability and fracture in hot forming.

References

[1] Harrison N R and Luckey S G 2014. Hot stamping of a B-pillar outer from high strength aluminum sheet AA7075 *SAE Int. J. Mater. Manuf.* **7** pp 567–73
[2] Xiao W, Wang B and Zheng K 2017. An experimental and numerical investigation on the formability of AA7075 sheet in hot stamping condition *Int. J. Adv. Manuf. Technol.* **92** pp 3299–09
[3] Kumar M and Ross N G 2017. Investigations on the hot stamping of AW-7921-T4 alloy sheet *Adv. Mater. Sci. Eng.* pp 1–10
[4] Ilinich A and Luckey S G 2014 On Modeling the hot stamping of high strength aluminum sheet *SAE Int.*
[5] D'Amours G and Ilinich A 2018 High temperature characterization and material model calibration for hot stamping of AA7075 aluminium sheet *J. Phys. Conf. Ser.* paper submitted
[6] D'Amours G 2004 *Développement de Lois Constitutives Thermomécaniques pour les Matériaux à Base de Carbone lors du Préchauffage d'une cuve d'électrolyse* Université Laval Québec
[7] Stoughton T B and Yoon J W 2011 Paradigm change : alternate approaches to constitutive and necking models for sheet metal forming AIP conference proceedingS 1383 pp 15-34
[8] 2018 *LS-DYNA Keyword User's Manual* **II** LSTC Livermore
[9] Hill R 1948 A Theory of the yielding and plastic flow of anisotropic metals *Math. Phys. Eng. Sci.* **193** pp 281–97
[10] Wang G, Qian X, Li X, Hou H, Liu Y and Lou Y 2014 A study on compressive anisotropy and nonassociated flow plasticity of the AZ31 magnesium alloy in hot rolling *Mathematical Problems in Engineering* **2014** pp 1–9
[11] Kami A, Bijan M D, Seyed ali S V, Dan-Sorin C and Banabic D 2014 Application of a GTN damage model to predict the fracture of metallic sheets subjected to deep-drawing. *P. Romanian Acad.* **15** pp 300-9
[12] Crisfield M A 1996 Non–Linear Finite Element Analysis of Solids and Structures **I**
[13] Andrade F X C, Feucht M, Haufe A and Neukamm F 2016 An incremental stress state dependent damage model for ductile failure prediction *Int. J. Fract.* **200** pp 127–50
[14] Bai Y and Wierzbicki T 2009 Application of extended Mohr–Coulomb criterion to ductile fracture *Int. J. Fract.* **161** pp.1–20